

Application of Response Surface Methodology in the Design of Functionally Graded Plasma Sprayed Hydroxyapatite Coatings

**Tanya J. Levingstone^{1,2,3}, Niall Barron⁴, Malika Ardhaoui⁵, Khaled Benyounis^{1,2,3},
Lisa Looney^{1,2,3}, Joseph Stokes^{1,2,3}**

¹ School of Mechanical and Manufacturing Engineering, Dublin City University, Dublin 9,
Ireland.

² Centre for Medical Engineering Research, Dublin City University, Dublin 9, Ireland

³ National Centre for Plasma Science and Technology, Dublin City University, Dublin 9, Ireland

⁴ National Institute for Cellular Biotechnology, Dublin City University, Glasnevin, Dublin
9, Ireland

⁵ Surface Engineering Research Group, School of Electrical, Electronic and Mechanical
Engineering, University College Dublin, Belfield, Dublin 4, Ireland.

Corresponding Author:

Dr. Tanya Levingstone

School of Mechanical and Manufacturing Engineering,

Dublin City University,

Dublin 9, Ireland.

tanya.levingstone@dcu.ie

Tel: 00 353 (0) 1 7007718

Fax: 00 353 (0) 1 7007148

24 **Abstract**

25 The highly complex process-property-structure relationship poses a major challenge in the
26 optimization of plasma sprayed hydroxyapatite coatings. In addition, contradictions in relation to
27 the ideal coating properties exist; a dense, highly crystalline coating is required for long term
28 coating stability, whereas coatings with lower crystallinity dissolve more rapidly but have an
29 improved osteogenic response *in vivo*. In this study, response surface methodology (RSM) is
30 utilized to investigate the influences and interaction effects of current, gas flow rate, powder feed
31 rate, spray distance and carrier gas flow rate on the roughness, crystallinity, purity, porosity and
32 thickness of plasma sprayed HA coatings. Roughness related to the particle velocity and particle
33 melting, and was highest at low gas flow rates and, due to the quadratic effect of current, at the
34 central current value. High crystallinity resulted at high current and low spray distance due to the
35 presence of bulk crystalline material and recrystallization of amorphous material. Purity was
36 highest at low carrier gas flow rate and high gas flow rate, where particle temperature was reduced.
37 Porosity was dependent on the degree of particle melting and was highest at low gas flow rate and
38 powder feed rate and at high current and spray distance. Coating thickness was determined by the
39 number of particles and the degree of flattening on impact, and was highest at high current, low
40 gas flow rate, high powder feed rate and low spray distance. From this in-depth analysis, predictive
41 process equations were developed and optimized to produce two distinct coatings; a stable coating
42 and a bioactive coating, designed to form the base and surface layers of a functionally graded
43 coating respectively, to provide enhanced osteogenesis, while maintaining long-term stability.
44 Culture of osteoblast-like cells on the coatings demonstrated an increased osteogenic response on
45 the bioactive coating compared to the other groups. Overall, this study identifies parameter effects
46 and interactions leading to the development of optimized coatings with the potential to enhance the
47 functional life of HA coated implants *in vivo*.

48 **Keywords**

49 Plasma spraying, hydroxyapatite, response surface methodology (RSM), functionally graded

50 coatings, *in vitro* response

51

52 1. Introduction

53 Hydroxyapatite (HA), a calcium phosphate bioceramic, has been widely used in orthopaedic and
54 dental applications as it has an almost identical chemical composition to that of the mineral
55 component of bone and has proven osteoconductive properties [1,2]. One such application is as a
56 coating for metallic hip implants, where it increases the rate of bone repair, provides enhanced
57 fixation of the implant to human bone, and protects the body from any metal-ion release from the
58 metallic implant [3,4]. Clinical results for HA coated implants demonstrate success in achieving
59 earlier bone ingrowth and fixation [5]. Lazarinis et al. reported survival rates for HA coated
60 implants of 98% at 10 years [6] and Sandiford et al. reported survival rates of 91.7% at 22.5 years
61 [7]. Over time HA coatings are naturally resorbed by the body; however, delamination or rapid
62 dissolution can result in implant failure [8-10]. Thus further improvements in HA coatings is
63 necessary in order to achieve the goal of lifelong functionality.

64
65 The stability of HA coatings is largely dependent on crystallinity and purity [11]. Within the body,
66 HA is degraded by two mechanisms, osteoclastic resorption and physiochemical dissolution [12].
67 These degradation processes negatively impact on the coating integrity leading to a weakened
68 coating with a reduced functional life. However, coating degradation has positive impacts on bone
69 formation, as dissolution of the coating leads to the release of calcium and phosphate ions, in the
70 form of Ca^{2+} , H_2PO_4^- , HPO_4^{2-} , PO_4^{3-} and $\text{CaH}_2\text{PO}_4^{4+}$, into the fluid surrounding the joint [10].
71 Proteins and ions activate the surface of the HA coating encouraging the precipitation of calcium
72 and phosphate as HA crystals [13,14]. Additionally, previous studies have shown that calcium and
73 phosphate released as a result of the degradation of calcium phosphate coatings can stimulate
74 osteoblast responses leading to more rapid mineralization [5,15]. Thus in determining the optimal
75 properties for calcium phosphate coatings, it is necessary to consider long term coating stability as

76 well as the immediate osteogenic responses to the coating when implanted. This study proposes
77 that a functionally graded coating containing two distinct layers, a stable base layer and a bioactive
78 surface layer, provides the ideal solution in achieving a hydroxyapatite (HA) coating with enhanced
79 bioactivity, while maintaining the long-term stability of the coated devices. Previous research into
80 functionally graded HA coatings focused on achieving enhanced coating adhesion through the
81 development of titanium/HA graded coatings [16,17]. This study presents a novel approach through
82 the use of RSM to develop optimized stable and bioactive coatings that can be functionally graded
83 to achieve an enhanced osteogenic response.

84
85 HA coatings are commonly deposited using atmospheric plasma spraying, a thermal spray process
86 in which powder particles are melted in a high temperature plasma jet and propelled towards a
87 substrate material to form a coating. This technique offers advantages including high coating
88 adhesion strength and a rapid coating deposition rate [8]. The process is affected by a large number
89 of process parameters and parameter interactions that are not fully understood or accounted for,
90 and as a result numerous contradictions in relation to the parameter effects on coating properties
91 are reported in the literature [18-23]. Thus in order to tailor the properties of the coating to meet
92 specific requirements, a detailed understanding of process-property-structure relationship is
93 required. Response surface methodology (RSM) consists of a collection of mathematical and
94 statistical tools used for designing experiments [24]. Representing a step forward from one-at-a-
95 time analyses, the method enables identification of optimal process parameters while deducing
96 interactive effects between process parameters. RSM approaches have been used to investigate a
97 range of plasma sprayed coatings including alumina, titanium dioxide, zirconia, and alumina-
98 titania [25-27] in addition to hydroxyapatite [21,22,28,29]. Our previous work examined the main
99 effects of current, gas flow rate, powder feed rate, spray distance and carrier gas flow rate on the
100 roughness, crystallinity and purity of plasma sprayed hydroxyapatite and identified parameter

effects and desirable parameter ranges for plasma spraying of HA coatings [30]. On a mechanistic level, each of these parameters we seen to ultimately influence two key aspects; the degree of particle melting within the plasma jet and the velocity at which particles impact the substrate surface. This study aims to bring about a clearer understanding of these complex relationships through further investigation of the process-property-structure relationships for plasma sprayed hydroxyapatite coatings and to develop process equations that will enable the development of optimized coatings that will form the stable base layer and bioactive surface layer of a functionally graded coating. The specific objectives of the study were to use RSM 1) to assess the effects of five process parameters: current (A), gas flow rate (B), powder feed rate (C), spray distance (D) and carrier gas flow rate (E), on the crystallinity, purity, roughness, porosity and thickness of plasma sprayed hydroxyapatite coatings; key properties that influence coating stability and cellular response upon implantation, 2) to develop predictive process equations that can identify the ideal process parameters required to produce a stable coating which will form the base layer of the functionally graded coating and a bioactive layer that will form the surface layer of the functionally graded coating and 3) to assess the osteogenic response to the developed coatings *in vitro*.

2. Experimental Methods

2.1. Experimental Design

The parameters and levels investigated in this study were selected based on the findings of an initial screening study of the process carried out by the authors [30]. The screening study analysed the effects of five parameters, (A) current (amps), (B) gas flow rate (standard cubic feet per hour (scfh)), (C) powder feed rate (g/min), (D) spray distance (mm) and (E) carrier gas flow rate (scfh), and found all five to significantly affect the investigated responses. All five parameters were thus included in the RSM study. Two levels were selected for each parameter based on the findings of

the screening study. A Central Composite Design (CCD) consisting of a 5^{-1} Fractional Factorial Design (16 experiments), with the addition of ten star point experiments and five centre point experiment to provide a measure of process stability and curvature, was used to investigate the effects of the various process parameters on the properties of HA coatings. The study was designed using the statistical software Design-Expert 7.0 (Stat-Ease Inc., Minneapolis, USA). The total number of experimental runs for the design was 31, as described in Table 1. The experiments were carried out in random order to remove the effects of systematic errors. Five coating responses were examined: roughness, crystallinity, purity, porosity and thickness. The main effects on each response were identified using the backward selection method to eliminate insignificant terms (P-value ≤ 0.01). The analysis of variance (ANOVA) test was used to determine the statistical significance of the developed equations. Statistical measures, R^2 , adjusted R^2 , predicted R^2 and adequate precision, were used to determine the adequacy of the resultant equations.

2.2. Materials

Titanium alloy (Ti, Ti6Al4V, grade 5, Impact Ireland, Dublin, Ireland) discs, 10 mm in diameter with a thickness of 2 mm, were used as the substrate material in this study. Prior to spraying, discs were grit-blasted at a pressure of 5 bar and an angle of incidence of 75° , using pure white Al_2O_3 grit with a particle size of 500 μm (mesh 36). High pressure air was used to remove and surface alumina particles and samples were then placed in dilute acetone in an ultrasonic cleaner for 5 minutes, rinsed in water and then dried. The average surface roughness (R_a) of the discs was 3.2 μm , as measured using surface profilometry (Surftest 402, Mitutoyo, Michigan, US). Hydroxyapatite (HA, $Ca_{10}(PO_4)_6(OH)_2$) powder with acrySTALLINITY of 99.96 % and purity of 99% was used (Captal 60-1 Thermal Spraying HA powder, Plasma Biotol, UK) [30]. The HA powder

148 had an irregular morphology and the particle size fell within two separate clusters, between 0.1 and
149 1.0 μm and between 10 and 100 μm , with a mean particle size of 38.3 μm [30].

150

151 2.3. Plasma Spraying

152 Plasma spraying was carried out using the Sulzer Metco 9MB plasmatron, fitted with a 3M7-GH
153 nozzle, as previously described [30]. High purity argon was used as both the plasma forming gas
154 and the powder carrier gas and no secondary gas was used. A traverse speed of 38 mm/s and a
155 spray time of 35 s were used for all coatings, resulting in 15 passes of the spray gun.

156

157 2.4. Coating Characterisation

158 Five parameters were investigated for each coating; roughness, crystallinity, purity, porosity and
159 thickness. Surface roughness, R_a , was measured using the Surftest 402 surface profilometer
160 (Mitutoyo, Michigan, US). Measurements were repeated four times with the sample orientation
161 changed between each measurement. The surface morphology of each coating was also examined
162 using scanning electron microscopy (SEM) (LEO 440 Stereo Scan, Leica, UK). The crystallinity
163 and purity of HA coatings were determined using x-ray diffraction (D-8 Advance Diffractometer,
164 Bruker, Coventry, UK) fitted with a copper anode. A locked-couple scan was carried out between
165 20 and 60° 2θ and an increment of 0.02 and a scan speed of 5 sec/step were applied. The %
166 crystallinity and % purity were calculated in accordance with ASTM F 2024-00 [31] using the
167 Diffract Plus EVA software (Bruker AXS, UK) as previously described [30]. In order to calculate
168 coating porosity and thickness, samples were sectioned longitudinally and mounted in resin
169 (Beuhler Epoxide Resin and Epoxide Hardner, mixed at a resin to hardner ratio of 5:1). Samples
170 were then ground and polished (Motopol 2000, Beuhler, Warwick, UK) and then cleaned in dilute
171 acetone solution to remove any remaining polishing debris. Samples were imaged at a

172 magnification of 20x for each specimen using the Reichert “MeF2” Universal Camera Optical
173 Microscope. Porosity measurements were carried out in accordance with the BSI standard 1071-5:
174 1995 [32]. Porosity was calculated using the Omninet Enterprise image analysis software (Beuhler,
175 Warwick, UK). Greyscale images were thresholded using an automated routine in order to
176 determine the percentage porosity for each coating. The Omninet Enterprise image analysis
177 software was also used to determine the coating thickness. Six measurements were taken for each
178 coating and an average obtained.

179

180 2.5. Assessment of model goodness of fit and optimization of process parameters

181 Following the development of process equations using the RMS, the model goodness of fit was
182 assessed using point prediction tests. Three new coatings were sprayed using parameters selected
183 randomly by the Design Expert software, detailed in Table 3, and the response values predicted by
184 the process equations were compared to the actual measured response values. The % error
185 between the predicted and actual values was obtained. Optimization of process parameters was
186 conducted using the Design Expert software by combining numerical simulation coupled with the
187 desirability function. The constraints applied in order to produce a stable coating and bioactive
188 coating and the identified optimal parameter settings for each are summarised in Table 4. These
189 settings were identified based on the desired roughness, crystallinity, purity, porosity and thickness
190 values from previous literature. The optimised coatings were then fabricated and characterised and
191 the results were compared to the values predicted by the developed process equations.

192

193 2.6. *In vitro* assessment

194 *In vitro* analysis was carried out to determine the osteoblast response to the optimized stable and
195 bioactive HA coatings in comparison to an uncoated Ti disc. MG-63 human osteoblast-like cells

196 (LGC Promochem, Middlesex, UK) were cultured in standard growth medium (Eagle's minimum
197 essential medium, supplemented with 10% fetal bovine serum, 1% non-essential amino acids, 1%
198 glutamine, 1% sodium pyruvate and 1% pen-strep) at 37°C and 5% CO₂. The Ti and HA-coated
199 discs were sterilized using dry heat at 160°C for 3 hours and placed in 24-well plates, prior to
200 seeding cells on the surface of the discs at a density of 10,000 cells per disc. Cell proliferation and
201 cell viability were analyzed at 7, 14, 21 and 28 day timepoints and gene expression was analyzed
202 at 7, 21 and 28 day timepoints. At each timepoint, cells were detached from the disc surface using
203 trypsin and then counted using a haemocytometer and a phase contrast microscope following trypan
204 blue exclusion.

205

206 2.6.1 *RNA Extraction and Quantification*

207 The expression of extracellular matrix (ECM) mineralization markers in MG-63 cells on the three
208 surfaces was determined by RNA extraction and quantitative real time PCR. Cells were lysed and
209 total RNA was isolated at each time point using the RNeasy Mini kit (Qiagen, UK). Total RNA
210 concentrations were determined spectrophotometrically at a wavelength of 260 nm on a
211 Nanodrop™.

212

213 2.6.2 *Quantitative Real-Time PCR*

214 The effect of the coating surfaces on the expression of alkaline phosphatase (ALP), type 1 collagen
215 (COL1) and osteocalcin (OC) was evaluated at each time point (Taqman, Applied Biosystems,
216 UK). Relative gene expression was carried out using the 7500 Fast Real-Time PCR System
217 (Applied Biosystems, Thermofisher Scientific, UK). Detection was achieved using Sybr Green
218 which is excited at 490 nm and emits at 520 nm. During the PCR reaction, samples were subjected
219 to an initial denaturation phase at 95°C for 20 s followed by 40 cycles of denaturation at 95°C for

220 3 s and annealing and extension at 60°C for 30 s. Glyceraldehyde phosphate dehydrogenase
221 (GAPDH) was used as the endogenous control.

222

223 2.6.3 Statistical Analysis

224 Statistical analysis for cell culture work was carried out using One-Way Anova to determine
225 significance (SigmaStat 3.0, Systat Software Inc., California, US). A p-value of < 0.05 represented
226 a significant difference.

227

228 3. Results

229 3.1. Measured Responses

230 The measured responses for each experimental run (N1-N31) are presented in Table 1. The average
231 roughness (Ra) ranged between 3.1 µm and 9.6 µm. SEM micrographs of cross-sections the
232 coatings with the lowest roughness (N11) and highest roughness (N30) are shown in Fig. 1(a) and
233 Fig. 1(b). The average crystallinity ranged between 71.2 % and 85% and the average purity ranged
234 between 93.8 % (N13) and 99.3 % (N12) as shown in Table 1. Overall, all coatings met the > 45
235 % crystallinity and > 95 % purity required by ISO 13779-2:2000 (Implants for surgery-
236 Hydroxyapatite. Coatings of hydroxyapatite) [33]. The average coating porosity ranged between
237 6.8 % (N8) and 59.1 % (N10). SEM micrographs of the surfaces of coatings N8 and N10 and shown
238 in Fig. 1(c) and Fig. 1(d) and cross-sections of the coatings N8 and N10 are shown in Fig 1(e) and
239 Fig. 1(f). The average coating thickness ranged from 17.2 µm to 543.5 µm. SEM micrographs of
240 cross-sections of the coatings for the lowest (N3) and highest (N6) thickness coatings are shown in
241 Fig 1(g) and Fig 1(h). The results were used to generate process equations, summarized in Table
242 2. Statistical measures for each parameter, also summarised in Table 2, indicate that there is a good

fit between the data and the equation for each response. The overall parameter effects for roughness, crystallinity, purity, porosity and thickness are summarized in the perturbation plots in Fig. 2.

3.2. Influence of process parameters on roughness

Roughness was found to be significantly affected by two parameters, current (A) and gas flow rate (B), and one interaction, between current and gas flow rate (A*B), as shown in Table 2 (P-value \leq 0.01). Gas flow rate (B) has the greatest influence, this was a linear relationship with increasing gas flow rate leading to a reduction in roughness. Current (A) was also seen to influence the coating roughness, a quadratic relationship was observed with higher currents leading to higher roughness values as can be seen in Fig. 3. The curvature of the current and roughness relationship indicates the roughness increases with increasing current up to a current of about 650 A, after which the roughness decreases again. The relative influence of these parameters on coating roughness is summarised in the perturbation plot in Fig. 2(a). The resultant regression equation for roughness is presented in Table 2 using actual parameters and coded parameters (where -1 and 1 represent the low and high levels).

3.3. Influence of process parameters on crystallinity

Crystallinity was found to be affected by current (A), gas flow rate (B), spray distance (D) and carrier gas flow rate (E). In addition, three interactions have an effect; current and gas flow rate (A * B), current and spray distance (A * D), and gas flow rate and carrier gas flow rate (B * E). Crystallinity was highest when the current was high, and gas flow rate, spray distance and carrier gas flow rate were all low as shown in Fig. 3. The relative influence of these parameters on coating

266 crystallinity is summarised in the perturbation plot in Fig. 2(b). The resultant regression equation
267 for crystallinity is presented in Table 2 using actual parameters and coded parameters.

268

269 3.4. Influence of process parameters on purity

270 The purity of the coating was found to be influenced by current (A), gas flow rate (B), powder feed
271 rate (C), spray distance (D) and carrier gas flow rate (E). Gas flow rate, carrier gas flow rate and
272 spray distance had the greatest effects with higher purity resulting when gas flow rate was high and
273 carrier gas flow rate and spray distance were low as shown in Fig. 4. The relative influence of these
274 parameters on coating purity is summarised in the perturbation plot in Fig. 2(c). The resultant
275 regression equation for purity is presented in Table 2 using actual parameters and coded
276 parameters.

277

278 3.5. Influence of process parameters on porosity

279 Coating porosity is influenced by current, gas flow rate, powder feed rate and spray distance. Gas
280 flow rate and powder feed rate had the greatest effect with higher levels of porosity resulting at low
281 gas flow rate and low powder feed rate as shown in Fig. 5. The relative influence of these
282 parameters on coating porosity is summarised in the perturbation plot in Fig. 2(d). The resultant
283 regression equation for porosity is presented in Table 2 using actual parameters and coded
284 parameters.

285

286 3.6. Influence of process parameters on thickness

287 Coating thickness was influenced by all parameters, with current and gas flow rate having the
288 greatest effect. Thicker coatings resulted at high current, high powder feed rate, high carrier gas

flow rate and low gas flow rate and spray distance as shown in Fig. 6. The relative influence of these parameters on coating thickness is summarised in the perturbation plot in Fig. 2(e). The resultant regression equation for thickness is presented in Table 2 using actual parameters and coded parameters.

3.7. Point prediction tests and process optimization

The point prediction tests demonstrate that the developed equations for each response accurately predict the actual measured response values (Table 3). The percentage error between the predicted and actual responses is very low ($< 5\%$) for crystallinity, purity and roughness. The average percentage error for the porosity and thickness equations was found to be higher ($< 11.5\%$) than for the other three responses. This is expected as the model statistics indicated that these equations have lower predictive power than the other equations developed as a result of the inherent variability identified within these responses in the centre point experimental runs. The percentage error found is still low enough to conclude that the model can predict the response value achieved. By applying the constraints identified in Table 4, the plasma spray process was optimized to produce two distinct coating with different properties depending on the optimization criteria used. The spray parameters used for each coating, the predicted and actual values for each response and percentage error are presented in Table 4Table 5.

3.8. *In vitro* assessment

3.8.1 *Cell proliferation and viability*

Biocompatibility was assessed by quantifying cell number and cell viability on the uncoated Ti, the stable coating and the bioactive coating. MG-63 osteoblast-like cells were seen to readily

proliferate on all surfaces with cell numbers seen to increase over the 28 day time period, thus indicating the biocompatibility of the surfaces under investigation. There was a trend towards higher cell numbers in the uncoated Ti group than the stable coating and bioactive coating groups at each timepoint although this was not significant (Fig.7(a)). High levels of cell viability were observed on all surfaces across all time points as shown in Fig.7(b), with no significant differences in viability observed between the groups.

3.8.2 *Gene Expression Analysis*

The expression of extracellular matrix mineralization markers type 1 collagen (COL1), alkaline phosphatase (ALP) and osteocalcin (OC) were determined using quantitative RT-PCR analysis. COL1, an early marker of mineralization which is expressed during cellular proliferation, was expressed by the MG-63 cells on each surface as shown in Fig. 8(a). At day 7, the highest level of COL1 expression is observed on the titanium surface. Expression of COL1 peaked at day 21, approximately a 2 fold increase was observed in all groups, with expression levels highest in the stable coating group. ALP, expressed during the osteoblast maturation stage, was highest in all groups at day 7, with higher levels observed in the HA coated groups compared to the uncoated Ti group. The expression of ALP for each surface at each time point is shown in Fig. 8(b). At day 28 no expression of ALP was observed on the stable coating or uncoated Ti groups; however, low levels of ALP expression were observed in the bioactive coating group. OC, expressed during the mineralization stage, was seen to be higher on the bioactive coating compared to the stable coating or uncoated Ti, with a 3.5 fold increase observed in this group at day 7. This demonstrates that the bioactive coating led to much earlier mineralization than the other groups. By day 21, OC expression was seen to be similar in all groups with expression levels remaining higher in the bioactive coating than in the other groups at the 28 day timepoint. The level of expression of

osteocalcin on each surface is shown in Fig. 8(c). This indicates that higher levels of mineralization occurred in the bioactive coating group than in the other groups.

4. Discussion

A major challenge exists in the design of optimized hydroxyapatite coated implants for dental and orthopaedic applications. On one hand, for long term coating stability, a dense highly pure, highly crystalline coating is required [34]; on the other hand, dissolution of the coating surface has been shown to lead to an improved *in vivo* response, resulting in an increase in the rate of bone formation [14]. This study used response surface methodology (RSM) to investigate the influences and interaction effects of current, gas flow rate, powder feed rate, spray distance and carrier gas flow rate on the roughness, crystallinity, purity, porosity and thickness of plasma sprayed HA coatings and demonstrated that all process parameters investigated significantly effect the properties of the resultant HA coatings. Process equations with high predictive power were developed in order to identify the ideal process parameters required to produce a stable coating and a bioactive coating, designed to be applied sequentially to form the base layer and surface layer respectively of a functionally graded coating.

The roughness of the fabricated HA coatings ranged from 3.1 μm and 9.5 μm and was influenced by current and gas flow rate with an interaction effect between current and gas flow rate. The results show that a lower gas flow rate increases particle melting due to an increased residence time within the plasma jet and thus particles undergo a greater degree of flattening on impact with the substrate leading to a lower coating roughness. The quadratic nature of the roughness response to current is clearly identified here bringing new clarity to previous conflicting findings [22,23,30,35]. The particle size distribution within the HA powder also likely has an important influence in this study,

360 with particle sizes falling within two separate clusters, between 0.1 and 1.0 μm and between 10 and
361 100 μm [30]. Thus at low current and high gas flow rate, the plasma jet is cooler and only smaller
362 particles are melted thus the coating roughness is lower. At low gas flow rate, and a current of up
363 to 650 A the number of larger particles being melted increases and thus the roughness increases.
364 After 650 A the degree of melting of the particles being deposited increases and the particles are
365 more molten and thus undergo a greater degree of flattening on impact. As can be observed from
366 the micrographs in Fig. 1, the high roughness coating is much thicker than the low roughness
367 coating, thus verifying that under the high roughness condition much greater numbers of particles
368 are deposited. Previous studies have shown that osteoblast attachment and differentiation was
369 greater on rougher HA coating [36,37]. In the development of optimized coatings, a stable coating
370 and a bioactive coating, high roughness values of 8.3 μm and 9.1 μm were achieved. Thus the
371 stable coating is designed to provide a greater surface area for attachment of the bioactive coating,
372 while for the bioactive coating is designed to increase the surface area for cell attachment and
373 coating dissolution and thus enable an enhanced osteogenic response as previously reported.

374

375 Coating crystallinity varied between 71.8 % and 85.2 %, and was highest at high current, low gas
376 flow rate, low spray distance and low carrier gas flow rate. Importantly, coating crystallinity in all
377 cases was > 45 % which is the requirement for biomedical applications [38]. The crystalline
378 fraction of a HA coating consists of bulk crystalline material from the unmelted central cores of
379 the HA particles and HA that has recrystallised following spraying [39]. Thus coating crystallinity
380 is dependant on the degree of particle melting and the particle cooling rate. It can be seen from the
381 interaction effects that high coating crystallinity results at high current, low gas flow rate and low
382 spray distance. These conditions cause an increase in particle melting and an increase in substrate
383 temperature, leading to a low particle cooling rate. The quantity of larger particles deposited is
384 greater, leading to the presence of a greater amount of bulk crystalline material within the coating,

385 resulting in a high % crystallinity. The low spray distance causes particle melting to be low due to
386 reduced residence time in the plasma jet. At low spray distance the substrate temperature is high
387 as it is closer to the plasma jet and thus cooling rate is low. The carrier gas flow rate determines
388 the entry positions of particles into the jet. At a low carrier gas feed rate particles do not enter the
389 center of the plasma jet, and as a result undergo less melting. In optimising coatings, crystallinity
390 was successfully maximised in the stable layer and minimised in the bioactive layer as coating
391 dissolution rates have been shown to be dependant on coating crystallinity [11].

392

393 The purity of the resultant coatings coating purity was found to vary between 96.1% and 99.7%
394 and thus all coatings had purities of > 95 % as required for medical devices [38]. From the
395 interaction plots it is clear that coating purity is dependent on the residence time of particles within
396 the plasma jet. As a result, purity is higher when the gas flow rate is high and the spray distance is
397 low and thus the particles spend less time in the plasma jet and remain at a lower temperature.
398 Cizek and Khor [22] previously investigated the relationship between HA particle in-flight
399 temperature and velocity and the loss of the HA phase in the resultant coatings and were not able
400 to identify any correlations. The findings in this study verify the relationship between phase
401 changes and particle melting proposed by Sun et al. [23]. The position of the particles within the
402 plasma jet also impacts on the coating purity, thus at low carrier gas flow rate fewer HA powder
403 particles enter the hotter centre region of the plasma jet and thus particle temperature remains
404 lower. In coating optimization, the resultant stable coating had a purity of 98.1% whereas the
405 bioactive coating had a purity of 96.1%. Coatings with higher purity have previously been shown
406 to have lower dissolution rates [11].

407

408 Porosity was found to vary between 6.8 % and 59.1 %. The porosity of a coating is dependent on
409 the degree of particle melting within the plasma jet and the amount of spreading on impact with

the substrate. Partially melted particles do not flatten completely, leaving gaps between them, resulting in a more porous coating. A highly molten particle that impacts the substrate at high speed spreads to a greater degree on the substrate thus reducing porosity [41]. Thus while a number of competing effects can be observed in the interaction plots, the overall effects in the perturbation plot show that porosity was highest at low gas flow rate, as this would result in lower particle impact velocity, and low powder feed rate, where less particles are deposited with each pass and thus a greater number of gaps exist between particles. Higher porosity also results at high current and high spray distance as a greater number of the larger particles are melted within the plasma jet under these conditions. These findings confirm the findings of Kweh et al. [20], who observed an increase in HA coating porosity at increased spray distances. Cizek and Khor [22] further investigated the relationship between porosity and in-flight velocity and temperature, however no significant trend was observed. A low porosity of 8.9% was successfully achieved in the stable coating with the aim of improving the mechanical stability of the coating [20]. Increased porosity of 47.3% was achieved in the bioactive coating, designed to allow a greater surface area for cell attachment and coating dissolution and to an enhanced osteogenic response following implantation as previously reported [34,42,43].

426

Coating thickness was found to range between 17.2 μm and 543.5 μm with thicker coating resulting at high current, low gas flow rate, high powder feed rate, low spray distance and high carrier gas flow rate. Coating thickness is known to be related to the number of particles that are deposited on the substrate surface and also the degree of flattening of the particles on impact, thus coating thickness also provides a measure deposition efficiency. The number of particles that are deposited on the substrate relates to the amount of particles that are fed into the plasma jet, the number of particles that are sufficiently melted within the jet to adhere to the substrate on impact and the number of particles that maintain sufficient velocity to remain in the plasma jet until the point of

435 impact. As expected, thicker coatings resulted at higher powder feed rates. Thicker coating also
436 resulted at high current and low spray distance under these conditions more particles are melted
437 within the plasma jet and the deposition efficiency is higher. Thicker coatings also result at low
438 gas flow rate and high powder feed rate and carrier gas feed rate. Under these conditions greater
439 numbers of particles enter the plasma jet leading to an increase in the number of particles deposited
440 on the substrate. A similar relationship between coating thickness and particle melting has been
441 reported by Sun et al. [23]. In the optimization process, coating thickness was successfully
442 maximized for both coatings resulting in a thickness of 391.4 μm for the stable coating and 232.5
443 μm for the bioactive coating.

444
445 The assessment of the cellular response to the optimized stable and bioactive coatings using MG-
446 63 osteoblast-like cells demonstrated an enhanced osteogenic response in the bioactive coating
447 group compared to the stable coating and uncoated Ti control groups. Cells were seen to readily
448 proliferate on all surfaces, indicating that all surfaces were biocompatible. Although not significant,
449 there is a trend towards higher levels of proliferation on the Ti surface to the 28 day timepoint while
450 on the HA coatings, lower levels of proliferation are observed, thus indicating that the cells in the
451 HA coating groups may enhance the matrix maturation or matrix mineralization phases of
452 osteoblast differentiation. There is no significant difference in the expression of earlier markers of
453 osteogenesis, collagen (COL1) and alkaline phosphatase (ALP), between the three groups.
454 Previous studies have shown that ALP expression was not affected by roughness [42], or HA purity
455 or calcium to phosphate (Ca/P) ratio [44]. A significant difference in osteocalcin (OC) expression
456 was observed at day 7 and day 28 with highest levels observed on the bioactive coating. Osteocalcin
457 is a marker of the mineralization phase of osteoblast differentiation and thus this indicates that the
458 bioactive coating promotes mineralization earlier than the titanium surface or stable coating. It is
459 noted that OC expression is higher in the Ti group than the stable coating group. This may be due

460 to the surface roughness of the Ti disc; enhanced osteogenesis on roughened Ti alloys has
461 previously been reported [45]. It is recognized that rapid osseointegration is crucial in order for an
462 implant to be successful *in vivo*, thus these results indicate that the bioactive coating provides the
463 most favorable conditions for bone formation. While this study indicates that the osteogenic
464 properties of the bioactive coating are enhanced compared to the uncoated Ti and the stable HA
465 coating, further *in vitro* analysis would be beneficial in order to fully elucidate the mechanisms
466 involved. These novel coatings also hold potential for the local delivery of advanced therapeutics
467 including drugs and biomolecules, designed to enhance osteoinduction, or antibiotics agents,
468 designed to prevent infection post implantation. Taken together these results demonstrate that
469 through process optimization the compositional and microstructural properties of plasma sprayed
470 hydroxyapatite coatings can be tailored to achieve coatings with increased stability, designed for
471 long term functionality, or with enhanced osteogenic properties and an ability to biologically
472 instruct and stimulate the regeneration of bone tissue at the implant site.

473 **5. Conclusions**

474 This study successfully used response surface methodology to identify the effects of current gas
475 flow rate, powder feed rate, spray distance, and carrier gas flow rate, on the crystallinity, purity,
476 roughness, porosity and thickness of plasma sprayed hydroxyapatite coatings; key properties that
477 influence coating stability and cellular response upon implantation. Consistent and competing
478 influences are identified enabling predictive process equations to be developed and optimized to
479 produce two distinct coatings, a stable coating and bioactive coating, designed to form the base and
480 surface layers respectively of a functionally graded coating. Through *in vivo* analysis enhanced
481 osteogenic response to the bioactive coating was demonstrated. The optimized coatings have the
482 potential to stimulate osteogenesis at the implant site and to enhance the functional life of HA
483 coated implants *in vivo*

484

485 **Acknowledgements**

486 The author would like to acknowledge the research support provided by the Irish Research Council
487 for Science, Engineering and Technology, funded by the National Development Plan.

488

489 **References**

490

491

Reference List

492 [1] R.Z. LeGeros, Properties of osteoconductive biomaterials: calcium phosphates. Clin. Orthop.
493 395 (2002) 81-98.

494 [2] R.Z. LeGeros, Calcium phosphate-based osteoinductive materials, Chem. Rev. 108 (2008)
495 4742-4753.

496 [3] S. Sousa, M. Barbosa, Effect of hydroxyapatite thickness on metal ion release from Ti6Al4V
497 substrates, Biomaterials. 17 (1996) 397-404.

498 [4] L. Sun, C.C. Berndt, K.A. Khor, H. Cheang, K.A. Gross, Surface characteristics and
499 dissolution behavior of plasma-sprayed hydroxyapatite coating, J. Biomed. Mater. Res. 62 (2002)
500 228-236.

501 [5] S. Vahabzadeh, M. Roy, A. Bandyopadhyay, S. Bose, Phase stability and biological property
502 evaluation of plasma sprayed hydroxyapatite coatings for orthopedic and dental applications,
503 Acta biomaterialia. 17 (2015) 47-55.

504 [6] S. Lazarinis, J. Kärrholm, N.P. Hailer, Effects of hydroxyapatite coating on survival of an
505 uncemented femoral stem: a Swedish Hip Arthroplasty Register study on 4,772 hips, Acta
506 orthopaedica. 82 (2011) 399-404.

507 [7] N. Sandiford, C. Doctor, S.S. Rajaratnam, S. Ahmed, D.J. East, K. Miles, A. Butler-Manuel,
508 J.A. Shepperd, Primary total hip replacement with a Furlong fully hydroxyapatite-coated titanium
509 alloy femoral component: Results at a minimum follow-up of 20 years, Bone Joint J. 95-B (2013)
510 467-471.

511 [8] L. Sun, C.C. Berndt, K.A. Gross, A. Kucuk, Material fundamentals and clinical performance
512 of plasma-sprayed hydroxyapatite coatings: a review, J. Biomed. Mater. Res. 58 (2001) 570-592.

513 [9] M. Nagano, T. Nakamura, T. Kokubo, M. Tanahashi, M. Ogawa, Differences of bone
514 bonding ability and degradation behaviour in vivo between amorphous calcium phosphate and
515 highly crystalline hydroxyapatite coating, Biomaterials. 17 (1996) 1771-1777.

516 [10] F. Fazan, P. Marquis, Dissolution behavior of plasma-sprayed hydroxyapatite coatings, J.
517 Mater. Sci. Mater. Med. 11 (2000) 787-792.

518 [11] P. Ducheyne, S. Radin, L. King, The effect of calcium phosphate ceramic composition and
519 structure on in vitro behavior. I. Dissolution, J. Biomed. Mater. Res. 27 (1993) 25-34.

520 [12] J.R. Davis, *Handbook of Materials for Medical Devices*, ASM International, Ohio, 2003.

521 [13] J. Weng, Q. Liu, J. Wolke, X. Zhang, K. De Groot, Formation and characteristics of the
522 apatite layer on plasma-sprayed hydroxyapatite coatings in simulated body fluid, Biomaterials. 18
523 (1997) 1027-1035.

524 [14] J. Morgan, K.R. Holtman, J.C. Keller, C.M. Stanford, In vitro mineralization and implant
525 calcium phosphate-hydroxyapatite crystallinity. Implant Dent. 5 (1996) 264-271.

526 [15] J. De Bruijn, C. Van Blitterswijk, J. Davies, Initial bone matrix formation at the
527 hydroxyapatite interface in vivo, J. Biomed. Mater. Res. 29 (1995) 89-99.

528 [16] C. Chen, T. Huang, C. Kao, S. Ding, Characterization of functionally graded
529 hydroxyapatite/titanium composite coatings plasma-sprayed on Ti alloys, Journal of Biomedical
530 Materials Research Part B: Applied Biomaterials. 78 (2006) 146-152.

531 [17] K. Khor, Y. Gu, C. Quek, P. Cheang, Plasma spraying of functionally graded
532 hydroxyapatite/Ti-6Al-4V coatings, Surface and Coatings Technology. 168 (2003) 195-201.

533 [18] R. Gadow, A. Killinger, N. Stiegler, Hydroxyapatite coatings for biomedical applications
534 deposited by different thermal spray techniques, Surface and Coatings Technology. 205 (2010)
535 1157-1164.

536 [19] G.A. Fielding, M. Roy, A. Bandyopadhyay, S. Bose, Antibacterial and biological
537 characteristics of silver containing and strontium doped plasma sprayed hydroxyapatite coatings,
538 Acta biomaterialia. 8 (2012) 3144-3152.

539 [20] S. Kweh, K. Khor, P. Cheang, Plasma-sprayed hydroxyapatite (HA) coatings with flame-
540 spheroidized feedstock: microstructure and mechanical properties, Biomaterials. 21 (2000) 1223-
541 1234.

542 [21] J. Cizek, K.A. Khor, Z. Prochazka, Influence of spraying conditions on thermal and velocity
543 properties of plasma sprayed hydroxyapatite, Materials Science and Engineering: C. 27 (2007)
544 340-344.

545 [22] J. Cizek, K.A. Khor, Role of in-flight temperature and velocity of powder particles on
546 plasma sprayed hydroxyapatite coating characteristics, Surface and Coatings Technology. 206
547 (2012) 2181-2191.

548 [23] L. Sun, C.C. Berndt, C.P. Grey, Phase, structural and microstructural investigations of
549 plasma sprayed hydroxyapatite coatings, Materials Science and Engineering: A. 360 (2003) 70-
550 84.

551 [24] C. Pierlot, L. Pawlowski, M. Bigan, P. Chagnon, Design of experiments in thermal spraying:
552 A review, *Surface and Coatings Technology*. 202 (2008) 4483-4490.

553 [25] T. Steeper, D. Varacalle, G. Wilson, W. Riggs, A. Rotolico, J. Nerz, A design of experiment
554 study of plasma-sprayed alumina-titania coatings, *J. Therm. Spray Technol.* 2 (1993) 251-256.

555 [26] B. Lin, M. Jean, J. Chou, Using response surface methodology for optimizing deposited
556 partially stabilized zirconia in plasma spraying, *Appl. Surf. Sci.* 253 (2007) 3254-3262.

557 [27] S. Forghani, M.J. Ghazali, A. Muchtar, A.R. Daud, N. Yusoff, C.H. Azhari, Effects of
558 plasma spray parameters on TiO₂-coated mild steel using design of experiment (DoE) approach,
559 *Ceram. Int.* 39 (2013) 3121-3127.

560 [28] N. Khun, Z. Li, K. Khor, J. Cizek, Higher in-flight particle velocities enhance in vitro
561 tribological behavior of plasma sprayed hydroxyapatite coatings, *Tribol. Int.* 103 (2016) 496-503.

562 [29] S. Dyshlovenko, L. Pawlowski, P. Roussel, D. Murano, A. Le Maguer, Relationship
563 between plasma spray operational parameters and microstructure of hydroxyapatite coatings and
564 powder particles sprayed into water, *Surface and Coatings Technology*. 200 (2006) 3845-3855.

565 [30] T.J. Levingstone, M. Ardhaoui, K. Benyounis, L. Looney, J.T. Stokes, Plasma sprayed
566 hydroxyapatite coatings: Understanding process relationships using design of experiment
567 analysis, *Surface and Coatings Technology*. 283 (2015) 29-36.

568 [31] Standard Practice for X-ray determination of phase content of plasma-sprayed
569 hydroxyapatite coatings", ASTM F 2024-00, ASTM International. (2000).

570 [32] Advanced technical ceramics-Methods of test for ceramic coatings: Part 5: Determination of
571 porosity, DD ENV 1071-5:1995, British Standards Institute. (1995).

572 [33] Implants for surgery- Hydroxyapatite. Coatings of hydroxyapatite, ISO 13779-2:2000
573 (2000).

574 [34] R.B. Heimann, Thermal spraying of biomaterials, *Surface and Coatings Technology*. 201
575 (2006) 2012-2019.

576 [35] K. Gross, M. Babovic, Influence of abrasion on the surface characteristics of thermally
577 sprayed hydroxyapatite coatings, *Biomaterials*. 23 (2002) 4731-4737.

578 [36] D.O. Costa, P.D. Prowse, T. Chrones, S.M. Sims, D.W. Hamilton, A.S. Rizkalla, S.J. Dixon,
579 The differential regulation of osteoblast and osteoclast activity by surface topography of
580 hydroxyapatite coatings, *Biomaterials*. 34 (2013) 7215-7226.

581 [37] R. Reid, B. Hall, I. Marriott, A. El-Ghannam, Early osteoblast responses to orthopedic
582 implants: Synergy of surface roughness and chemistry of bioactive ceramic coating, *Journal of*
583 *Biomedical Materials Research Part A*. 103 (2015) 1961-1973.

- 584 [38] Standard Specification for Composition of Ceramic Hydroxyapatite for Surgical Implants,
585 ASTM F1185-03 , ASTM International. (2003).
- 586 [39] T. Kim, Q. Feng, Z. Luo, F. Cui, J. Kim, Highly adhesive hydroxyapatite coatings on
587 alumina substrates prepared by ion-beam assisted deposition, *Surface and Coatings Technology*.
588 99 (1998) 20-23.
- 589 [40] Implants for surgery- hydroxyapatite. Part 1: Ceramic hydroxyapatite, BS ISO 13779-
590 1:2000, International Organisation for Standards. (2000).
- 591 [41] C. Quek, K. Khor, P. Cheang, Influence of processing parameters in the plasma spraying of
592 hydroxyapatite/Ti-6Al-4V composite coatings, *J. Mater. Process. Technol.* 89 (1999) 550-555.
- 593 [42] D.D. Deligianni, N.D. Katsala, P.G. Koutsoukos, Y.F. Missirlis, Effect of surface roughness
594 of hydroxyapatite on human bone marrow cell adhesion, proliferation, differentiation and
595 detachment strength, *Biomaterials*. 22 (2000) 87-96.
- 596 [43] M. Rouahi, E. Champion, P. Hardouin, K. Anselme, Quantitative kinetic analysis of gene
597 expression during human osteoblastic adhesion on orthopaedic materials, *Biomaterials*. 27 (2006)
598 2829-2844.
- 599 [44] S. Best, B. Sim, M. Kayser, S. Downes, The dependence of osteoblastic response on
600 variations in the chemical composition and physical properties of hydroxyapatite, *J. Mater. Sci.*
601 *Mater. Med.* 8 (1997) 97-103.
- 602 [45] E. Chikarakara, P. Fitzpatrick, E. Moore, T. Levingstone, L. Grehan, C. Higginbotham, M.
603 Vázquez, K. Bagga, S. Naher, D. Brabazon, In vitro fibroblast and pre-osteoblastic cellular
604 responses on laser surface modified Ti-6Al-4V, *Biomedical Materials*. 10 (2014) 015007.

605
606

Tables

Table 1: Response surface methodology design showing levels of the variables under investigation and the average values of the measured responses.

Key	Exp Name	Variables					Responses (Average Values)				
		A	B	C	D	E	Roughness	Crystallinity	Purity	Porosity	Thickness
		A	slpm/scfh	g/min	mm	slpm/scfh	μm	%	%	%	μm
Fractional Factorial Experiment Runs	N1	550	42/90	10	70	9.4/20	8.1	73.3	96.4	19.2	94
	N2	750	42/90	10	70	4.7/10	8.7	82.7	99	24	375.4
	N3	550	71/150	10	70	4.7/10	4	72.5	99.1	-	17.2
	N4	750	71/150	10	70	9.4/20	7.6	81	98.5	16.3	265.4
	N5	550	42/90	20	70	4.7/10	8.8	80.4	97.6	12.7	286.1
	N6	750	42/90	20	70	9.4/20	8.8	79.7	97.8	6.9	543.5
	N7	550	71/150	20	70	9.4/20	5.7	72.4	98.3	29.5	85.4
	N8	750	71/150	20	70	4.7/10	7.7	85	98.6	6.8	182.8
	N9	550	42/90	10	100	9.4/20	8.1	82.3	96.8	34.4	122.4
	N10	750	42/90	10	100	9.4/20	8	73.8	95.4	59.1	153.5
	N11	550	71/150	10	100	9.4/20	3.1	74.2	97.1	-	30.2
	N12	750	71/150	10	100	4.7/10	5.5	71.2	99.3	6.8	48
	N13	550	42/90	20	100	9.4/20	8.4	76.5	93.8	16.7	137.3
	N14	750	42/90	20	100	4.7/10	8.5	80.1	97.1	36.2	346.2
	N15	550	71/150	20	100	4.7/10	4.2	73.2	98.8	-	17.4
	N16	750	71/150	20	100	9.4/20	8.1	79.6	97.3	11.2	211.7
Star Point Runs	N17	550	57/120	15	85	7.1/15	6.8	78.3	97.8	11.6	42.6
	N18	750	57/120	15	85	7.1/15	7.9	80.3	98.9	12.3	320.2
	N19	650	42/90	15	85	7.1/15	7.5	80.4	97.1	30.2	276.2
	N20	650	71/150	15	85	7.1/15	8.5	79.4	97.9	15.7	52.5
	N21	650	57/120	10	85	7.1/15	7.3	81.1	97.9	23.5	193.4
	N22	650	57/120	20	85	7.1/15	5.8	81.8	97	9.7	271.5
	N23	650	57/120	15	70	7.1/15	8.8	76.9	98.3	29.7	300.8
	N24	650	57/120	15	100	7.1/15	8.9	77.4	97.3	11.3	104.2

	N25	650	57/120	15	85	4.7/10	7.6	74.1	98.4	8	114.8
	N26	650	57/120	15	85	9.4/20	9.5	76.7	98.3	36.7	246.2
Centre Point Experiment Runs	N27	650	57/120	15	85	7.1/15	7.6	76.5	97.8	29.2	213.6
	N28	650	57/120	15	85	7.1/15	8.1	78.9	97.5	12.8	194
	N29	650	57/120	15	85	7.1/15	6.8	74.7	97.4	15.2	211.7
	N30	650	57/120	15	85	7.1/15	9.6	80	97.8	10.9	309.7
	N31	650	57/120	15	85	7.1/15	7.2	76.2	97.8	24.2	193.2

Table 2: Coded and actual experimental equations for roughness, crystallinity, purity, porosity and thickness. In the coded factor equations -1 and 1 represent the low and high levels.

Response	Coded and Actual Regression Equations	Eqn. No.	Statistical Measures					
			R ²	Adjusted R ²	Predicted R ²	Adequate Precision	F-Value	p-value
Roughness	Roughness = + 7.95 + 0.86 * A – 1.27 * B + 0.71 * A*B -0.84 * A ²	Eqn. 1	0.74	0.7	0.63	14.12	18.28	<0.0001
	Roughness = - 9.73718 + 0.089639 * current – 0.19524 * gas flow rate + 2.35417E-004 * current * gas flow rate - 8.40598E-005 * current ²	Eqn. 2						
Crystallinity	Crystallinity = + 77.69 + 1.10 * A – 1.57 * B – 1.56 * D -1.21 *E + 1.21 *A*B - 2.19 *A*D + 1.50 *B*E	Eqn. 3	0.75	0.67	0.54	12.65	9.64	<0.0001
	Crystallinity = 58.23267 +0.086458 * current - 0.46512 * gas flow rate + 0.84421 * spray distance - 1.44222 * carrier gas flow rate + 0.000404167 * current * gas flow rate - 1.45833E-003 * current * spray distance + 0.01 * gas flow rate * carrier gas flow rate	Eqn. 4						

Purity	Purity = +98.37 + 0.12 * A + 0.52 * B - 0.081 * C - 0.37 * D - 0.55 * E - 0.12 * A*D - 0.13 * B*C + 0.35 * B*D - 0.17 * D*E	Eqn. 5	0.91	0.87	0.77	22.42	25.72	<0.0001
	Purity = 97.68237 + 6.00833-3 * Current - 0.014327 * gas flow rate - 0.021512 * spray distance + 0.029722 * carrier gas flow rate - 0.0000603125 * Current * spray distance - 0.000760714 * gas flow rate * powder feed rate + 0.00050625 * gas flow rate * spray distance - 1.74375E-003 * spray distance * carrier gas flow rate	Eqn. 6						
Porosity	Porosity = +19.20 + 1.18 * A - 6.58 * B - 5.81 * C - 0.76 * D - 4.12 * A*B + 7.12 * A*D - 10.17 * B*D	Eqn. 7	0.68	0.57	0.42	12.47	6.08	0.0007
	Porosity = -15.52858 - 0.22733 * current + 2.59389 * gas flow rate - 1.16269 * powder feed rate - 0.42552 * spray distance - 1.37202E-003 * current * spray distance - 0.022605 * gas flow rate * spray distance	Eqn. 8						
Thickness	Thickness = +190.19 + 89.67 * A - 79.11 * B + 43.46 * C - 50.81 * D + 14.26 * E - 27.02 * A*D - 26.95 * B*C + 33.07 * B*E	Eqn. 9	0.87	0.82	0.71	19.13	18.66	<0.0001
	Thickness = -888.26428 + 2.42781 * current - 3.24889 * gas flow rate + 30.25178 * powder feed rate + 8.32107 * spray distance - 23.60044 * carrier gas flow rate - 0.18013 * current * spray distance - 0.17966 * gas flow rate * powder feed rate + 0.22044 * gas flow rate * carrier gas flow rate	Eqn. 10						

Table 3: Parameter settings for prediction point tests and model goodness of fit results

	<i>Coating</i>	<i>Current (A)</i>	<i>Gas Flow Rate (B)</i>	<i>Powder Feed Rate (C)</i>	<i>Spray Distance (D)</i>	<i>Carrier Gas flow rate (E)</i>
		<i>A</i>	<i>SCFH</i>	<i>g/min</i>	<i>mm</i>	<i>SCFH</i>
	1	600	120	10	80	17
	2	700	100	15	90	12
	3	600	110	20	85	15
	<i>Coating</i>	<i>Roughness (μm)</i>	<i>Crystallinity (%)</i>	<i>Purity (%)</i>	<i>Porosity (%)</i>	<i>Thickness (mm)</i>
Predicted Value	1	8	77.3	97.9	26.4	124.3
Actual Value		7.6	77.4	98.5	24.1	105.9
Error %		5	0.13	0.61	8.64	14.8
Predicted Value	2	9.1	79.5	97.9	34.9	293.3
Actual Value		9.4	78.3	98.5	29.9	281.6
Error %		3.19	1.5	0.61	14.33	3.99
Predicted Value	3	8.5	78.6	97.8	16.8	255.3
Actual Value		8.5	78.8	98.4	15.2	215.2
Error %		0	0.25	0.61	9.52	15.7
Average Error %		2.73	0.63	0.61	10.85	11.5

Table 4: Process optimisation goal and importance settings for the stable coating and bioactive coating. The optimisation criteria for the stable coating aim to produce a long lasting coating that will remain stable for long periods in the body, whereas the optimisation criteria for the bioactive coating aim to enhance the osteogenic response *in vivo*.

	Stable Coating		Bioactive Coating	
	<i>Goal</i>	<i>Importance</i>	<i>Goal</i>	<i>Importance</i>
Roughness (μm)	Maximize	+++	Maximize	+++
Crystallinity (%)	Maximize	+++++	Minimize	+++++
Purity (%)	Maximize	++++	Minimize	+++++
Porosity (%)	Minimize	++++	Maximize	+++++
Thickness (μm)	Maximize	+	Maximize	+

Table 5: Parameter levels and measured responses for the optimised stable coating and bioactive coating. The optimal parameter levels identified for each coating are presented with the predicted and actual values for each response and percentage error.

<i>Stable Coating</i>					
Parameter		Response	Predicted	Actual	% Error
Current (A)	750	Roughness (μm)	8.6	8.3	3.5
Gas Flow Rate (slpm/scfh)	49.9/104.8	Crystallinity (%)	84.7	84.4	0.3
Powder Feed Rate (g/min)	20	Purity (%)	98.5	98.1	0.4
Spray Distance (mm)	70	Porosity (%)	6.3	8.9	29.1
Carrier Gas flow rate (slpm/scfh)	4.7/10	Thickness (μm)	414	391.4	5.4
<i>Bioactive Coating</i>					
Parameter		Response	Predicted	Actual	% Error
Current (A)	750	Roughness (μm)	8.9	9.1	2.4
Gas Flow Rate (slpm/scfh)	42.5/90	Crystallinity (%)	72.7	74.6	2.5
Powder Feed Rate (g/min)	10.2	Purity (%)	95.7	96.1	0.4
Spray Distance (mm)	100	Porosity (%)	53	47.3	10.8
Carrier Gas flow rate (slpm/scfh)	9.4/20	Thickness (μm)	266.4	232.5	12.7

Figure captions

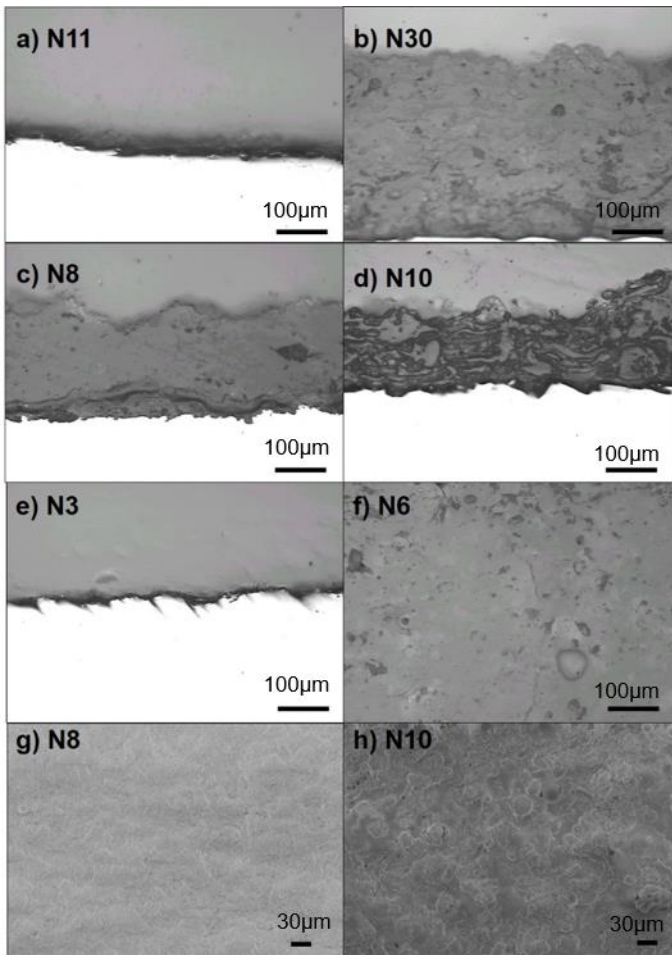


Figure 1: SEM micrographs showing the cross-sectional images of the coatings with the a) the lowest roughness (N 11) and b) the highest roughness (N30), c) the lowest porosity (N8) and d) the highest porosity (N10) e) the lowest thickness (N3) and f) the highest thickness (N6) and SEM micrographs of the surface of the coatings with the g) lowest porosity (N8) and h) highest porosity (N10). Scale bars for (a) to (f) represent 100 μm and for (g) and (h) represent 30 μm

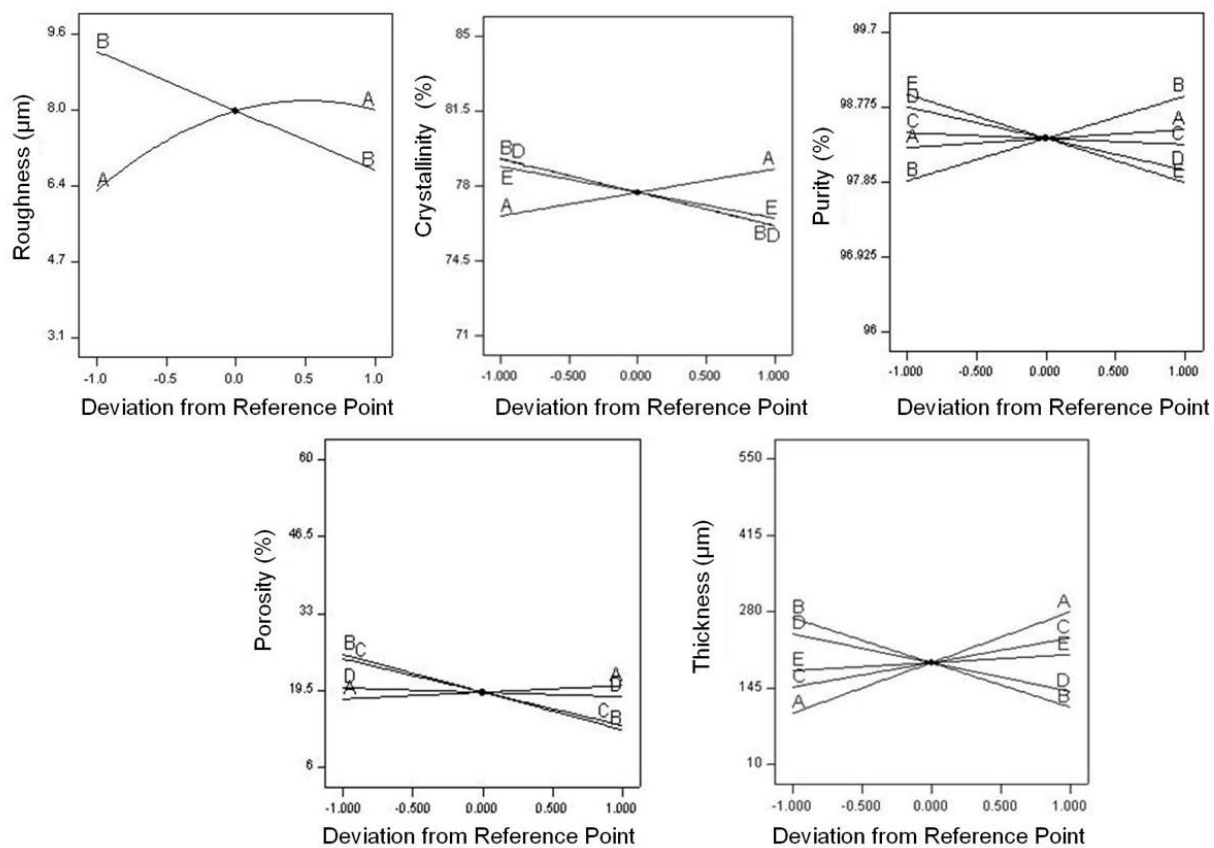


Figure 2: Perturbation plots showing the main effects of Current (A), Gas Flow Rate (B), Powder Feed Rate (C), Spray Distance (D) and Carrier Gas Flow Rate (E) on a) roughness, b) crystallinity, c) purity, d) porosity and e) thickness

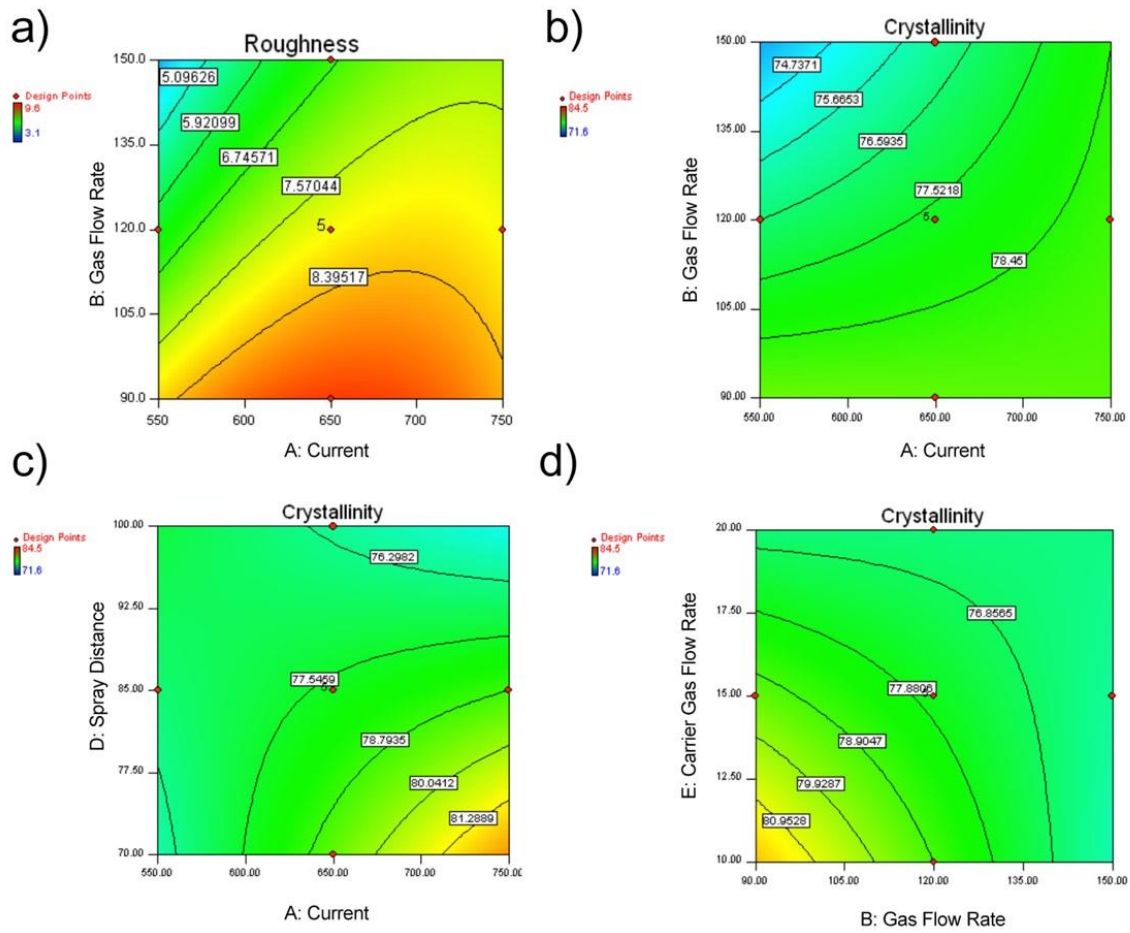


Figure 3: Interaction effect of a) current * gas flow rate on roughness b) current * gas flow rate on crystallinity c) current * spray distance on crystallinity and d) gas flow rate * carrier gas flow rate on crystallinity

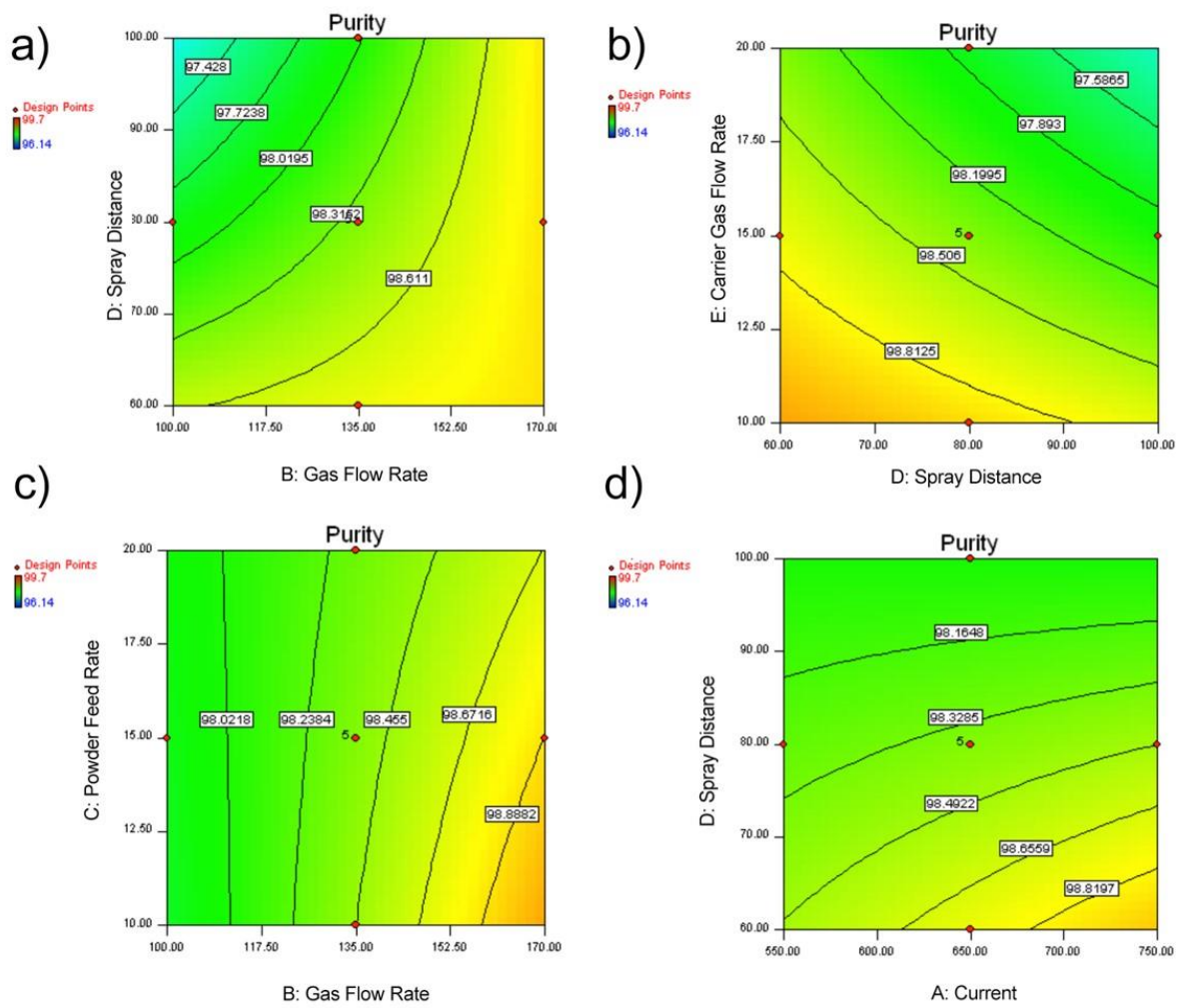


Figure 4: Interaction effect of a) gas flow rate * spray distance b) spray distance * carrier gas flow rate c) gas flow rate * powder feed rate and d) current * spray distance on purity

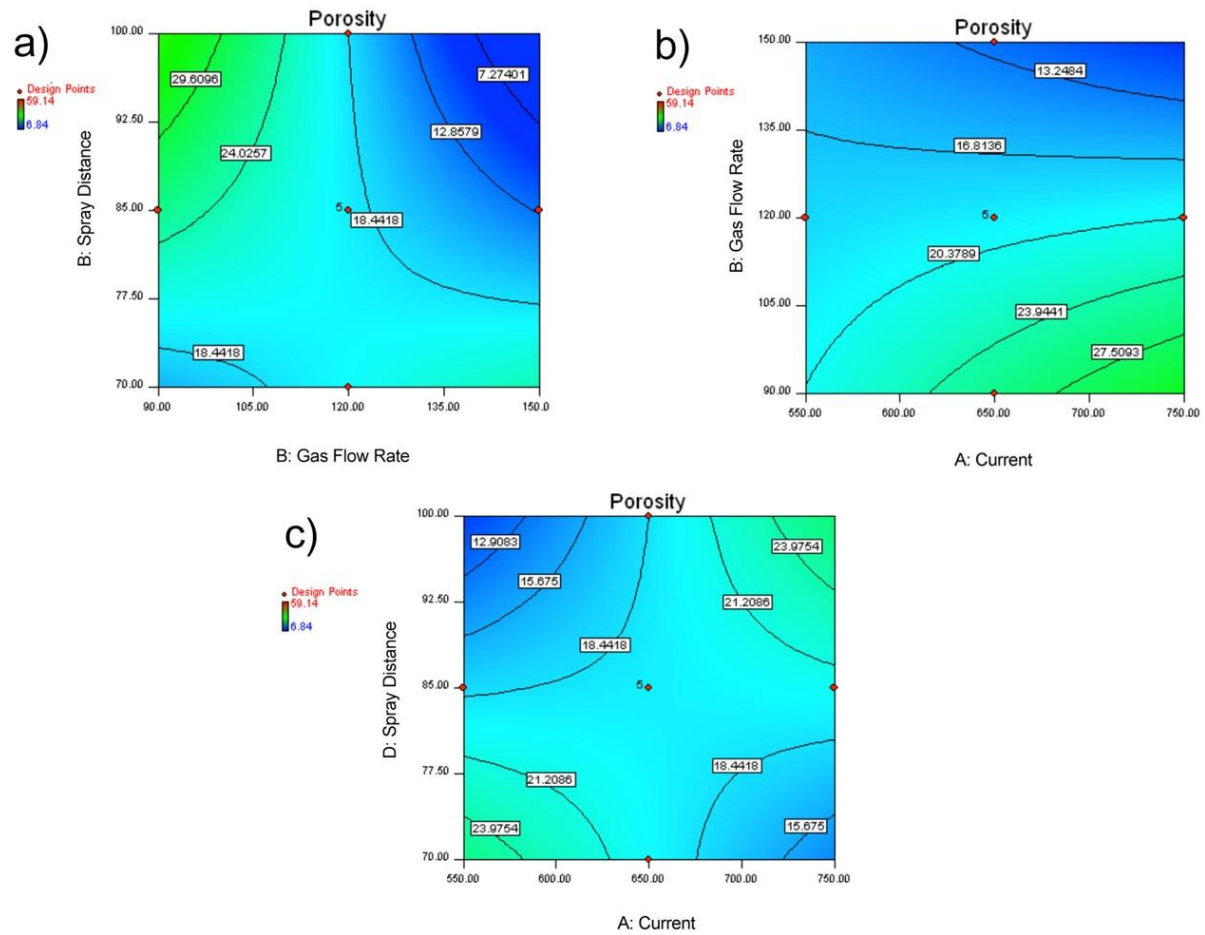


Figure 5: Interaction effect of a) gas flow rate * spray distance b) current * gas flow rate and c) current * spray distance on porosity

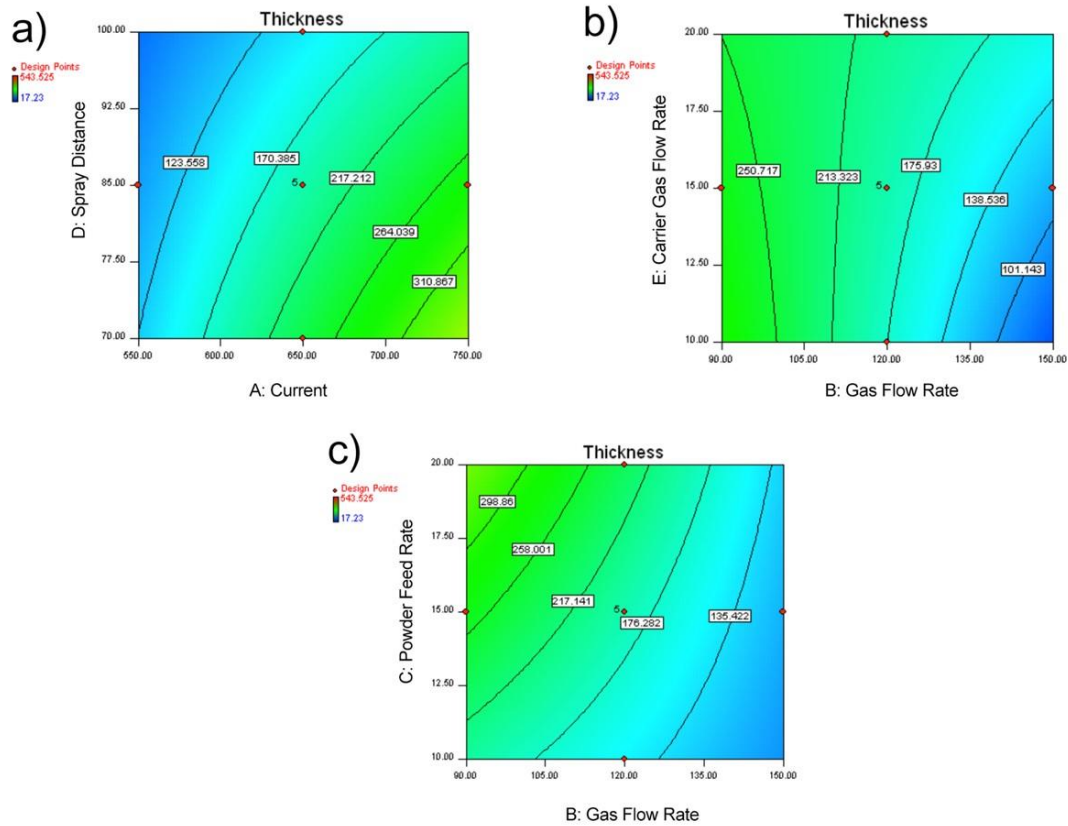


Figure 6: Interaction effect of a) current * spray distance b) gas flow rate * carrier gas flow rate and c) gas flow rate * powder feed rate on thickness

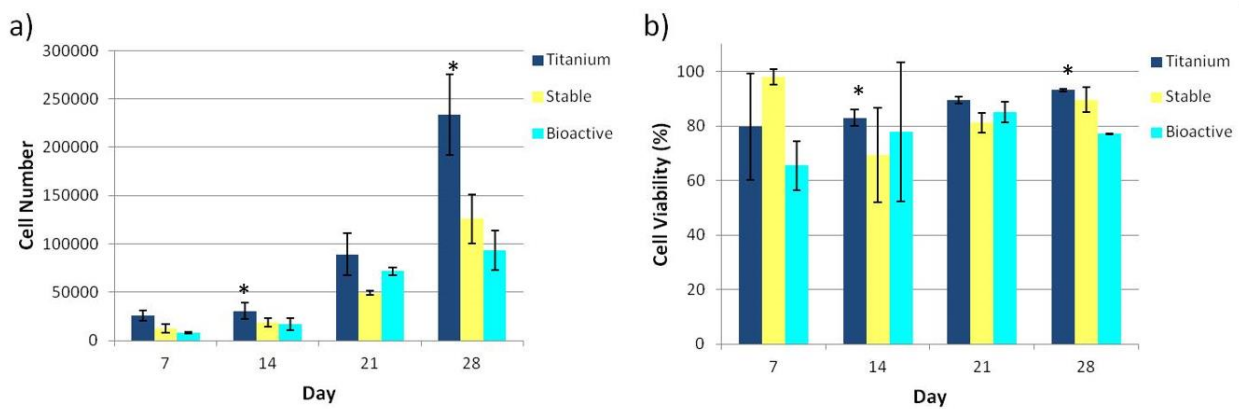


Figure 7: Cell proliferation and cell viability on the titanium control, stable coating and bioactive coating at day 7, 14, 21 and 28 (* indicates p < 0.1)

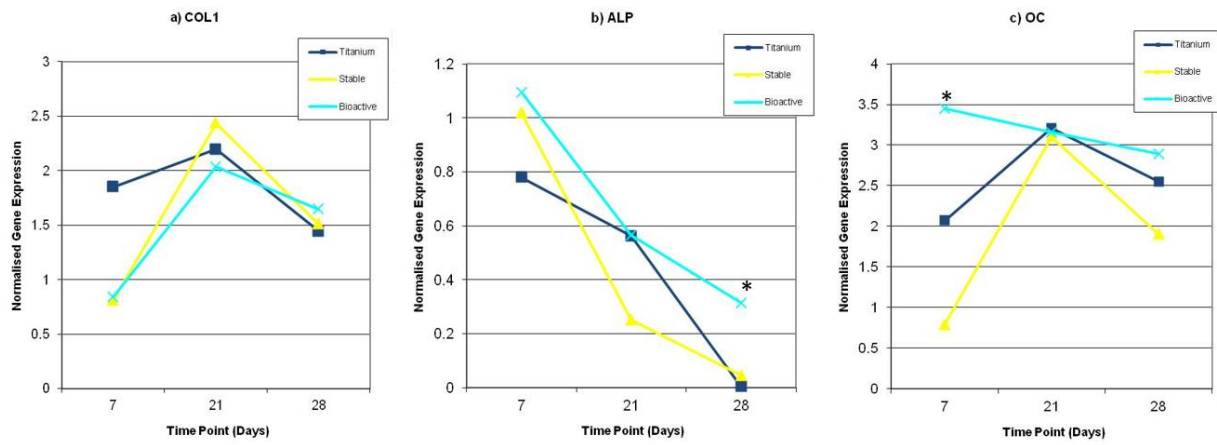


Figure 8: Gene expression profiles for a) collagen 1 (COL1), b) alkaline phosphatase (ALP) and c) osteocalcin (OC) on the titanium control, stable coating and bioactive coating at day 7, 21 and 28 (* indicates $p < 0.05$)